Research Square

Preprints are preliminary reports that have not undergone peer review.
They should not be considered conclusive, used to inform clinical practice,
or referenced by the media as validated information.

Real-time dual-telescope normalization for absorption muography: an improved density estimation approach

Hamid Basiri

basiri.hamid@gmail.com

The University of Tokyo https://orcid.org/0000-0002-4360-0327

Jun Matsushima

Masashi Kodama

Toshiyuki Yokota

Mohammed Ali

Kalifa University https://orcid.org/0000-0001-7502-3897

Fateh Bouchaala

Ahmed Khaled Eleslambouly

Khalifa University of Science and Technology https://orcid.org/0009-0005-9029-0666

Hiroyuki K.M. Tanaka

Eduardo Cortina Gil

Andrea Giammanco

Article

Keywords:

Posted Date: November 24th, 2025

DOI: https://doi.org/10.21203/rs.3.rs-7921528/v1

License: This work is licensed under a Creative Commons Attribution 4.0 International License.
Read Full License

Additional Declarations: There is **NO** Competing Interest.

Version of Record: A version of this preprint was published at Communications Physics on November 2nd, 2026. See the published version at https://doi.org/10.1038/s42005-026-02921-z.

Real-time dual-telescope normalization for absorption muography: an improved density estimation approach

Hamid Basiri[1*], Jun Matsushima[1], Masashi Kodama[1,2], Toshiyuki Yokota[2], Mohammed Y. Ali[3], Fateh Bouchaala[3], Ahmed Eleslambouly[3], Hiroyuki K.M. Tanaka[4], Eduardo Cortina Gil[5], Andrea Giammanco[5]

[1]Department of Environment Systems, Graduate School of Frontier Sciences, The University of Tokyo, Tokyo, Japan.

[2]Geological Survey of Japan, National Institute of Advanced Industrial Science and Technology (AIST), Japan.

[3]Department of Earth Sciences, Khalifa University of Science and Technology, Abu Dhabi, United Arab Emirates.

[4]Earthquake Research Institute, The University of Tokyo, Tokyo, Japan.

[5]Centre for Cosmology, Particle Physics and Phenomenology, Université catholique de Louvain (UCLouvain), Chemin du Cyclotron 2, Louvain-la-Neuve, B-1348, Belgium.

[*] *Corresponding author*

Email: Basiri.hamid@edu.k.u-tokyo.ac.jp; basiri.hamid@gmail.com.

Abstract

Absorption muography infers path-averaged density from the attenuation of atmospheric muons; however, transient flux variations due to weather, solar activity, and geomagnetism bias sequential measurements that rely on non-simultaneous backgrounds. We demonstrate real-time dual-telescope normalization using two identical plastic scintillator–PMT telescopes operated in parallel: one views open sky (reference), the other the target (main). Their count-rate ratio cancels common-mode flux changes and tracks detector drift. A 140-h no-target run yields a stable calibration, and stacked acrylic slabs give an empirical transmission–thickness curve. Minimum-ionizing events are selected with a robust valley-bounded pulse-height window. Transmissions are

fitted with a weighted exponential and cross-checked by a Bayesian variant. Applied to blind targets, the dual-mode recovers the densities of 20-cm aluminum and 10-cm stainless-steel blocks within uncertainties, whereas a single-telescope workflow shows significant biases. A compact vertical stack improves common-mode rejection. The method reduces systematics and is directly applicable to field deployments.

Introduction

Cosmic-ray muons are produced in the upper atmosphere and reach the ground with GeV energies[1,2]. Due to their penetration power, muons can pass through hundreds of meters of rock, making them a desirable tool for imaging the internal density of various targets[2]. This technique, known as muography or muon radiography, exploits the fact that muons travel in nearly straight-line trajectories at relativistic speeds and interact mostly by ionization, meaning any attenuation of the flux of muons is proportional to and a measure of the quantity and composition of the material that muons passed through[1,3]. Muography techniques are divided into absorption and scattering muography[4,5]. Absorption muography is optimal for mapping large-scale structures, where the attenuation of muons represents the density distribution[6]. Muography has been used in various applications, e.g., imaging the inner structures of volcanoes[7-10], mining and ore[11-13], archaeology[14,15] and cultural-heritage studies[16,17], civil engineering[18,19], magnetic field monitoring[20,21], carbon capture storage sites[22,23], mineral deposits, and rock density investigations[24,25], nuclear waste monitoring[26], and nuclear reactor imaging[27,28].

In this study, we used plastic scintillators coupled with photomultiplier tubes (PMTs). Plastic-scintillator-based detectors, optically read by PMT or by silicon photomultipliers (SiPMs), have been used in various practical applications of muography[29-37]. These detectors typically have lower spatial resolution than emulsions and gaseous trackers, but they offer significant practical advantages. They are mechanically robust, low-cost, and scalable to large areas; operate reliably under harsh field conditions; and provide immediate electronic readout (real-time acquisition) with nanosecond-scale timing (fast response)[3,38]. Additionally, plastic scintillators can be fabricated in application-specific geometries (e.g., via extrusion, machining, or 3D printing), allowing for compact or custom telescope layouts[38-40]. Moreover, scintillator panels are easily assembled into

telescope arrays and can be stacked in multiple layers to obtain the muon trajectory by coincidence timing.

The cosmic-ray muon flux at sea level, which averages about 1 cm^{-2} min^{-1}, is subjected to temporal variations due to changes in atmospheric pressure and temperature, geomagnetic disturbances, and solar–heliospheric activity[41,42]. The most prominent variations are meteorological[43,44]. An increase in atmospheric pressure compresses the air column, increasing the probability that parent pions and kaons will interact before they can decay into muons, which reduces the muon flux at the surface. This "barometric effect" is quantified by a coefficient of approximately -0.1% per hPa, meaning that a 10 hPa pressure increase causes 1% decrease in flux[45]. Values around 0.13 –0.15% hPa^{-1} are also reported for surface muon telescopes[46]. Additionally, changes in stratospheric temperature modulate the muon flux; a warmer stratosphere is less dense, allowing more pions to decay into muons, thus increasing the surface flux. This temperature effect can induce seasonal flux variations of 1–3%[42,47]. In addition to these predictable meteorological influences, solar and geomagnetic conditions can induce more abrupt and irregular variations in muon flux. Coronal mass ejection (CME), which is a large eruption of magnetized plasma from the Sun, often produces a short-term drop in the galactic cosmic-ray flux known as a Forbush decrease (FD)[48]. CMEs and associated magnetic storms produce short-term percent-level depressions in the ground-level muon flux (approximately 1–3%, with rare events approaching 10%)[49]. These depressions typically last from days to over a week, after which the cosmic-ray flux gradually recovers. Changes in the Earth's geomagnetic field, such as geomagnetic storms accompanying solar events, can further affect the low-energy cosmic-ray cutoff rigidity, slightly altering the muon flux, especially at lower latitudes.

All of the environmental factors mentioned above can introduce noise into the muon flux. The measured muon count rate can vary by comparable magnitudes to the attenuation rate from a density anomaly of interest. Specifically, in joint muography and seismic invesion[50], the uncertainties in density estimation from muography will directly propagate into seismic calculations of shear and bulk moduli. Therefore, the transient flux fluctuations must be carefully corrected to isolate the absorption signal of muons' propagation through the internal structure. Moreover, muography provides a path-integrated mean density, making it challenging to resolve or isolate localized density variations along a specific section.

Conventional methods to correct for the cosmic-ray muon variations often rely on analytical models that use environmental data, such as barometric pressure and atmospheric temperature profiles[41,51]. This method involves continuously recording the local barometric pressure and, if possible, the effective atmospheric temperature (using balloon sounding or global models) and then normalizing the muon counts to constant reference conditions. Such pressure-temperature corrections can stabilize long-term muon flux measurements[41-44,51,52]. However, model-based pressure/temperature corrections have important limits. The coefficients depend on detector, energy threshold, and geometry, so treating them as constants can bias results. Temperature terms require the full vertical profile (effective temperature), and model choice, location/time mismatch, and data delays introduce biases, making real-time correction difficult. Simple linear regressions often leave residual variance; a principal component analysis (PCA) approach using pressure, along with the full temperature profile, performs better but remains imperfect[51]. Meteorology-only corrections also miss non-meteorological transients (e.g., Forbush decreases), and their responses vary with zenith angle. A single correction factor across a wide field leaves angle-dependent residuals that can mimic structure imaging, and therefore, it requires angle-binned corrections or a matched acceptance reference. Finally, these schemes do not account for detector efficiency drifts or run-to-run differences, when open-sky and target data are collected in different runs or with different instruments, additional normalizations are required. Therefore, the common practice of forming simultaneous transmission ratios with a co-located reference view[2].

While model-based corrections can reduce variance, they remain imperfect, require external data, and fail to account for non-meteorological transients or detector-specific drift. This capability gap motivates a direct, empirical normalization. To address this, we propose and validate a dual-telescope normalization method. In this setup, two identical telescopes are operated: a “reference” telescope records the open-sky background flux and serves as a stable baseline real-time reference, while a “main” telescope measures the muon flux transmitted through the target simultaneously. By taking the ratio of the simultaneous measurements from the two telescopes, transient flux variations common to both are effectively canceled in real-time. This approach provides a direct, empirical normalization that is insensitive to the source of the flux variation and enhances the accuracy of the resulting density estimation. In this study, we experimentally demonstrate the

effectiveness of this dual-telescope methodology for real-time normalization, highlighting its advantages for improving the reliability and precision of density estimations in muography.

Results

Ratio stability and cross-calibration

From the 140-hour background run (with no target), we calculated the hourly count rates for the main and reference telescopes, as well as their ratio, $T_{\mathrm{dual}}(t)$. The calibration coefficient (C_{cal}) is defined as the time-average of this ratio. Figure 1a shows the hourly rates summarized as a moving average with 6-h binned mean ± the standard error of the mean (SEM), and Fig. 1b the Main/Reference ratio; the dashed line is the overall mean used as the calibration coefficient. We obtain $C_{\mathrm{cal}} = 0.965$, implying that the main telescope registers about 3.5% fewer counts than the reference under identical conditions. The hour-to-hour scatter of $T_{\mathrm{dual}}(t)$ about the mean (visible in Fig. 1b) quantifies the stability of the cross-calibration, and its standard deviation is taken as the uncertainty on C_{cal}.

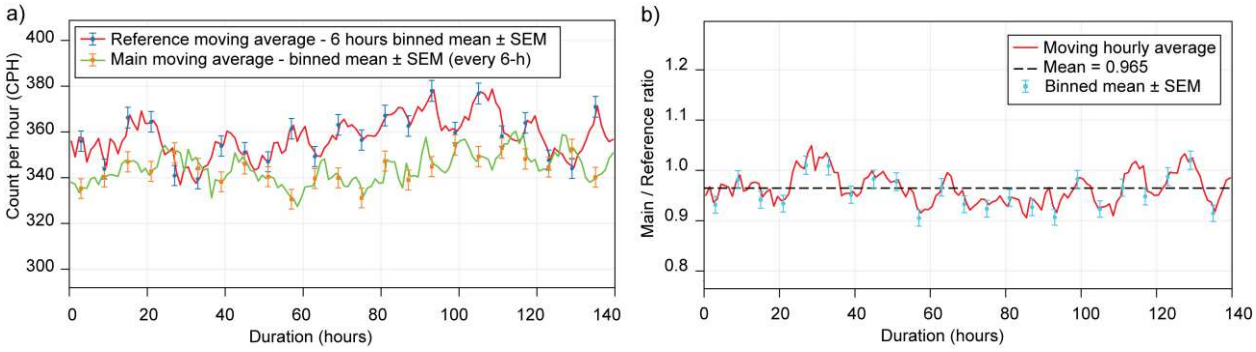


Figure 1 | Determination of the calibration coefficient from the background run. (a) Hourly rates for the reference and main telescopes are summarized as moving-average curves (lines) with 6-h binned mean ± SEM (markers). (b) Main/Reference ratio vs time (line: moving average; markers: 6-h binned mean ± SEM). The dashed line is the overall mean $C_{\mathrm{cal}} = 0.965$, used as the calibration coefficient.

Transmission measurements on acrylic and blind targets

For each acrylic stack with thicknesses of 20 cm, 40 cm, 60 cm, and 80 cm, we formed hourly counts and computed transmissions using both single- and dual-telescope approaches. Figure 2a represents the acrylic measurement in each main and reference telescope. After acrylics, we measured an aluminum target of 20 cm × 20 cm × 20 cm and a stainless-steel target of 20 cm × 20 cm × 10 cm as blind targets for the density estimation. We report the time average ⟨T⟩ and its

uncertainty as SEM. Uncertainties include Poisson statistics and the appropriate propagated error. Table 1 lists the acrylic calibration points together with the measured transmissions for the blind targets.

Table 1 | Measured transmissions (time-averaged) in dual and single modes. Uncertainties represent 1σ SEM and include propagation of C_{cal} (Dual) or the background baseline $R_{0\,main}$ in Single mode.

Sample	Thickness x (cm)	$\langle T_{dual} \rangle \pm$ SEM	$\langle T_{single} \rangle \pm$ SEM
Acrylic	20	0.9388 ± 0.0043	0.9407 ± 0.0031
Acrylic	40	0.9022 ± 0.0041	0.9100 ± 0.0030
Acrylic	60	0.8941 ± 0.0038	0.8846 ± 0.0028
Acrylic	80	0.8787 ± 0.0042	0.8722 ± 0.0031
Aluminum	20	0.9075 ± 0.0042	0.8971 ± 0.0030
Stainless Steel	10	0.8915 ± 0.0047	0.9002 ± 0.0035

Density recovery using the acrylic calibration

Using the transmissions in Table 1, we fitted an exponential fit to the acrylic attenuation model in equation (8) separately for the dual and single modes and mapped the measured transmissions through aluminum (d = 20 cm) and stainless steel (d = 10 cm) to densities. Uncertainties on ρ propagate the standard errors of the mean (SEM) of the target transmissions and the (A, μ) covariance from the acrylic fit for the corresponding mode. For stainless steel, multiple scattering and secondary production could deflect a small fraction of tracks from the main toward the reference telescope, which would raise R_{ref} and bias the dual ratio T_{dual} low. In our setup, the main and reference acceptances do not overlap, and each telescope requires a tight threefold coincidence, so the probability that such tracks satisfy the reference trigger is negligible.

Table 2 reports the recovered densities. We also quote a Z-score, $Z \equiv (\rho - \rho_{ref})/\sigma_\rho$, where ρ_{ref} is the reference (true) density and σ_ρ is the 1σ uncertainty of the recovered density; $|Z| \lesssim 1$ indicates consistency within 1σ. In dual mode, both targets agree with their reference values within uncertainties (Al: $Z = +0.04$, SS: $Z = -0.68$). In single mode, aluminum is biased upward by $\sim$ 19% ($Z = +3.24$) and stainless steel downward by $\sim$ 23% ($Z = -4.99$), consistent with residual non-stationarity when no simultaneous reference is used. Figure 2b summarizes the estimated

density and the relative errors. A Bayesian cross-check of the acrylic fit yields central values consistent with the exponential fit, albeit with slightly larger uncertainties (by ~approximately 5–10%); we omit these numbers for brevity.

Table 2 | Recovered densities using the exponential fit to acrylic (per mode). Reference values: $\rho_{AI} = 2.70$ g cm^{-3}, $\rho_{SS} = 7.90$ g cm^{-3}.

Mode	Aluminum ($d = 20$ cm)			Stainless Steel ($d = 10$ cm)		
	ρ (gcm^{-3})	$\Delta\rho/\rho_{ref}$ (%)	Z	ρ (gcm^{-3}) (%)	$\Delta\rho/\rho_{ref}$	Z
Dual	2.710±0.267	0.38	0.04	7.483±0.612	−5.28	−0.68
Single	3.212±0.158	18.95	3.24	6.097±0.361	−22.82	−4.99

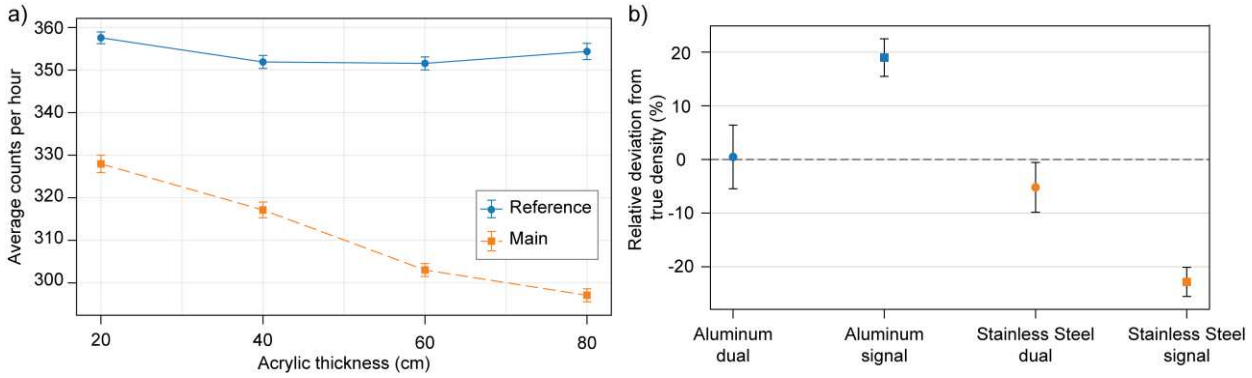


Figure 2 | Muon counts versus acrylic thickness and density estimation errors. (a) Hourly MIP-selected counts for the main and reference telescopes are shown as a function of path length (x). These data provide the basis for the Dual and Single transmission estimates and the exponential fit $T(x) = Ae^{-\mu x}$. (b) Densities for aluminum (20 cm) and stainless steel (10 cm) are derived from the acrylic calibration using dual and single modes. Relative errors are calculated with respect to reference values of 2.70 and 7.90 g cm^{-3}, respectively.

Effect of telescope alignment

We quantified how relative placement affects common–mode rejection by acquiring long no-target runs in two geometries: (i) the original side-by-side layout and (ii) a vertical stack with the reference telescope directly above the main. Both runs used identical DAQ settings, the same automated valley MIP selection, and 1h time binning over a 111-hour window.

Figures 3a and 3b compare the CPH time series for the two layouts. The higher CPH in the vertical design reflects the different inter-plane distances (refer to Figs. 4 and 8). To quantify temporal synchrony, we first used the Pearson correlation of the hourly CPH series (defined as

equation 1), which ranges from −1 (perfect negative correlation) to +1 (perfect positive correlation). Figures 3c-3d show scatter plots of hourly CPH (main vs. reference) for the two layouts. Each point is one hour (n = 111), and the dashed line indicates $y = x$. The side-by-side case shows a weak, non-significant correlation (r = −0.053, p = 0.578), whereas the vertical stack exhibits a modest but significant positive correlation (r = 0.197, p = 0.038), indicating more coherent hour-by-hour co-variation in the stacked geometry.

$$r = \frac{\sum_{t=1}^{n}(R_{main}(t) - \overline{R}_{main})\,(R_{ref}(t) - \overline{R}_{ref})}{(\sqrt{\sum_t (R_{main}(t) - \overline{R}_{main})^2}(\sqrt{\sum_t (R_{ref}(t) - \overline{R}_{ref})^2}}, \quad (1)$$

We also summarize stability with the coefficient of variation (CV) of any rate series $R(t)$ as

$$CV(R) = \frac{\sigma_R}{\mu_R} \times 100\%, \quad (2)$$

where μ_R and σ_R are the mean and standard deviation of $R(t)$. For CPH, the vertical stack yields nearly identical and low relative spreads for reference and main (about 2.6% and 2.5%), whereas side-by-side shows lower absolute rates and larger relative spreads (~ 5%).

Finally, we calculated the calibration ratio coefficient (C_{cal}). The results are presented in Figs. 3d and 3e, showing that the vertical stacking layout brings the scale closer to unity and reduces variability. C_{cal} increases from 0.959 ± 0.073 (CV 7.6%) for side-by-side to 0.992 ± 0.033 (CV 3.3%) for the vertical layout. The fraction of hours within ±5% and ±2% of unity increases from 50.5% to 90.1% and from 16.2% to 41.4%, respectively.

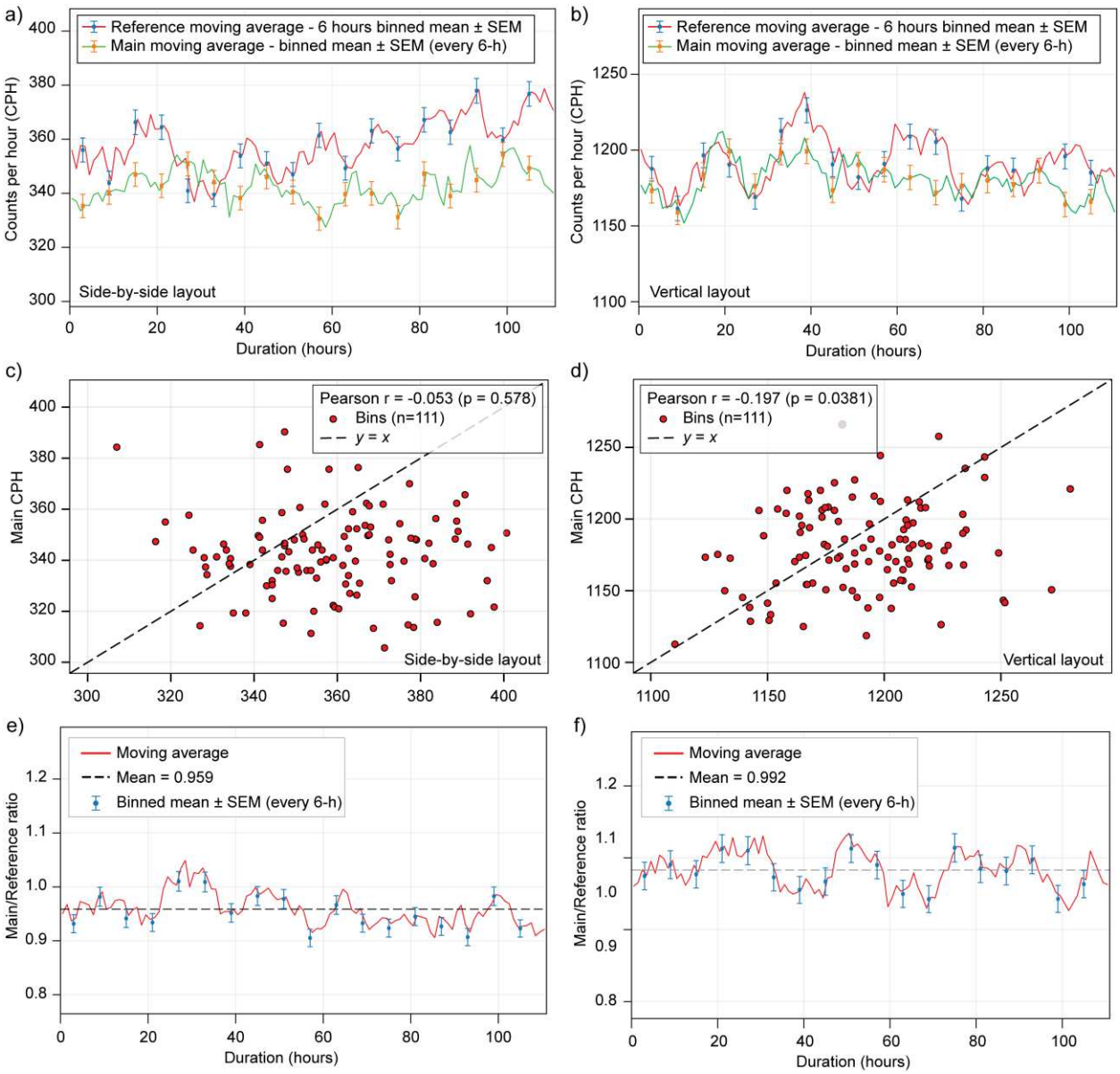


Figure 3 | Comparison of main and reference telescope count rates under two geometries. (a) Side-by-side layout showing hourly CPH data with 6 h moving averages and 6 h binned means ± SEM. (b) Vertical layout with similar processing, illustrating higher absolute CPH values due to differing inter-plane distances. (c) Side-by-side layout: main versus reference CPH ($n = 111$); dashed line represents $y = x$, with a correlation coefficient $r = -0.053$, $p = 0.578$. (d) Vertical layout: main versus reference CPH ($n = 111$); dashed line represents $y = x$, with a correlation coefficient $r = 0.197$, $p = 0.038$. (e) Ratio of main to reference detector rates for side-by-side layout. (f) Ratio of main to reference detector rates for vertical layout. The dashed lines in panels e and f represent the mean value, defined as the calibration coefficient.

Table 3 | Alignment metrics (valley cuts; 1 h bins; 111 h window). Means are shown with CV in parentheses.

Metric	Side-by-side	Vertical
$\langle R \rangle \pm$ SD (CV)	0.959 ± 0.073 (7.6%)	0.992 ± 0.033 (3.3%)
% within ± 5% of unity	50.5%	90.1%
% within ± 2% of unity	16.2%	41.4%
r (p)	−0.053 (0.578)	0.197 (0.038)
Ref mean CPH (CV)	357.89 (5.3%)	1164.22 (2.6%)
Main mean CPH (CV)	344.92 (4.8%)	1164.37 (2.5%)

Therefore, vertical stacking improves cross-calibration (mean ratio nearer to 1 and lower CV), yields a larger calibration coefficient close to unity, and shows significantly more coherent hour-scale tracking ($r > 0$ with $p < 0.05$). These features translate into stronger common–mode rejection in practice.

Discussion

We introduced simultaneous dual-telescope normalization for absorption muography that removes run-to-run flux variability without relying on external meteorological data. The approach requires only a co-aligned open-sky reference and a short no-target calibration. Thereafter, a count-rate ratio tracks common-mode flux changes and detector drift in real time.

In the laboratory tests, this ratio substantially reduced systematic bias in density estimates. The dual-mode recovered aluminum (20 cm) at 2.71 ± 0.27 g cm^{-3} (Z = +0.04) and stainless steel (10 cm) at 7.48 ± 0.61 g cm^{-3} (Z = −0.68), whereas the conventional single-telescope baseline showed biases of +18.95% and −22.82%, respectively. A vertical stack modestly improved common-mode rejection relative to a side-by-side layout, thereby tightening the calibration ratio from 0.959 ± 0.073 to 0.992 ± 0.033.

A single effective exponential adequately fits the transmission–thickness relation in our narrow-acceptance laboratory geometry, and a Bayesian cross-check yields compatible parameters with broader intervals due to correlation propagation. For wider acceptances or heterogeneous scenes, the same ratio strategy can be applied in angular bins to avoid zenith-dependent residuals. If

required, small post-ratio residuals can be regressed against pressure and an effective temperature proxy as a secondary clean-up rather than a primary control.

In practice, the field workflow is straightforward. Run the open-sky reference continuously with acceptance matched to the main view as closely as feasible. Before or during a campaign, take a short no-target check to set C_{cal} and record its coefficient of variation as a quality gate. From the ratio in angular bins for imaging, apply the same mapping from transmission to density, as validated in this study. If ambient residuals remain, apply a light regression on pressure and effective temperature to the binned ratios.

The approach has limits that follow from its assumptions. The ratio cancels only truly common-mode changes. Acceptance mismatch and wide fields leave angle-dependent residuals unless the ratio is binned by angle. The reference must remain open-sky and stable; partial occlusion, local shielding, or moving equipment can bias it. PMT gain drift can shift the mean ratio between checks, which suggests the need for periodic no-target verification and simple run-quality thresholds on the hourly ratio distribution. Time resolution is statistics-limited, so thin or weakly attenuating targets may require longer integrations.

These properties make the method well-suited to long-term monitoring under changing weather or solar conditions where false positives from transients are costly. Typical use cases include volcano and geothermal opacity tracking, civil and geotechnical assets, subsurface voids and tunneling, CO_2 storage measurement, monitoring, verification (MMV), mining backfill and pillar verification, and facilities where the reference view can be kept free of occludes. The workflow is estimator-agnostic and transfers directly from the laboratory to the field.

Conclusions

We validated a dual-telescope, real-time normalization for absorption muography using two identical scintillator–PMT telescopes operated in parallel that cancel transient muon-flux variations and improve density estimation accuracy. A 140-hour background run provided a stable cross-calibration (C_{cal} = 0.965), and stacked acrylic established an effective transmission model. Applied to blind targets, the dual-mode recovered densities were consistent with reference values (Al 20 cm: 2.71 ± 0.27 g cm^{-3}; SS 10 cm: 7.48 ± 0.61 g cm^{-3}), whereas the conventional single-

telescope workflow showed larger biases (+18.95% for Al and −22.82% for SS). A compact vertical stack modestly increased hour-scale coherence and tightened the calibration ratio (0.992 ± 0.033 vs 0.959 ± 0.073), though the dominant gain comes from using a simultaneous reference. Together, these results provide a practical, field-ready pathway to accurate real-time density retrieval in deployments where absolute density is crucial.

Methodology

Telescopes

We operated two identical plastic-scintillator telescopes in parallel. Each telescope consisted of three 20×20×2 cm^3 polystyrene tiles, each optically coupled to a PMT, forming three detector units (hereafter "channels"). A photograph of a detector unit and the key parameters of detector components are shown in Supplementary Information, Fig. 1 and Table 1. The three channels were stacked and read out in three-fold (3/3) coincidence to select through-going muons. One telescope ("main") viewed the target, while the other ("reference") viewed the open sky. A 20×20×3 cm^3 Pb plate mounted immediately below the top planes ranged out MeV electrons and attenuated MeV gamma rays, leaving GeV muons essentially unaffected. Figure 4 shows the dual-telescope setup. All measurements were conducted indoors on the fourth floor of a seven-story building, using identical DAQ settings. Unless noted, count rates are reported as counts per hour (CPH) and uncertainties are 1σ.

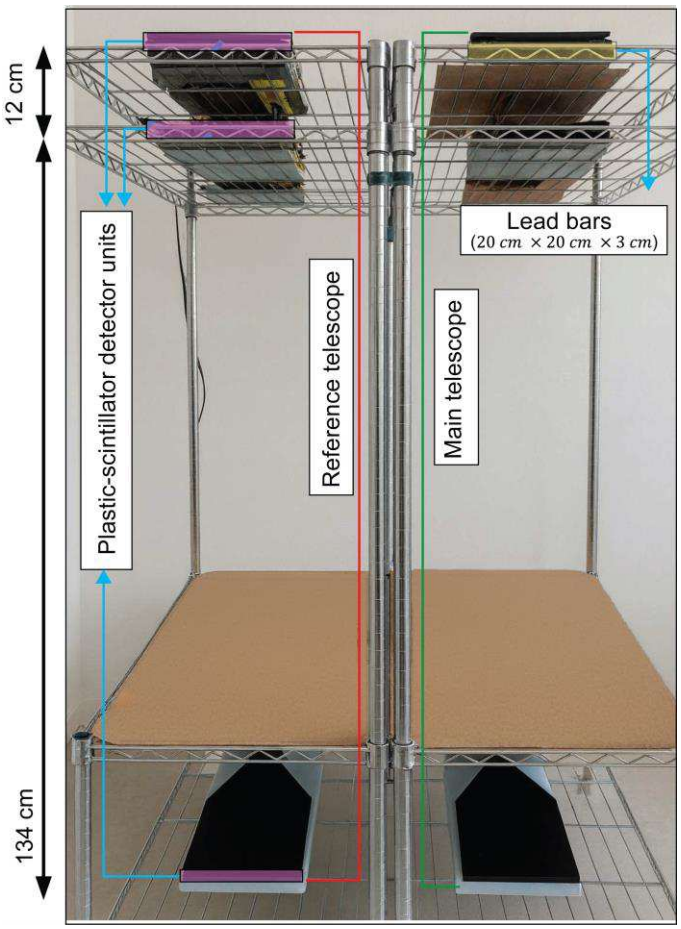


Figure 4 | Dual-telescope setup. Two identical three-plane scintillator–PMT modules are operated simultaneously. The main telescope views the target, while the reference telescope views the open sky. A 20 cm × 20 cm × 3 cm Pb plate placed below the top planes attenuates MeV electrons and gamma rays while leaving GeV muons essentially unaffected.

Signal processing and data acquisition chain

Each PMT is biased at approximately 1.5 kV by a high-voltage (HV) supply and delivers an analog signal proportional to detected pulses. PMT output signals are split into two synchronized paths. In the timing/trigger path, analog pulses are discriminated, and a three-fold (3/3) coincidence across the three channels defines a valid muon event, opening a short gate. In parallel, the pulse-height path amplifies and digitizes the signals. The digitizer is externally gated by coincidence, so only through-going events are binned in the multichannel analyzer (MCA). Figure 5a summarizes the chain, and Figs. 5b and 5c show the DAQ layout and. The same thresholds and gate settings were held fixed for all runs. Hourly counts per channel are obtained by integrating the MIP window

into the gated spectra and then summing over the three channels of each telescope to form counts per hour (CPH).

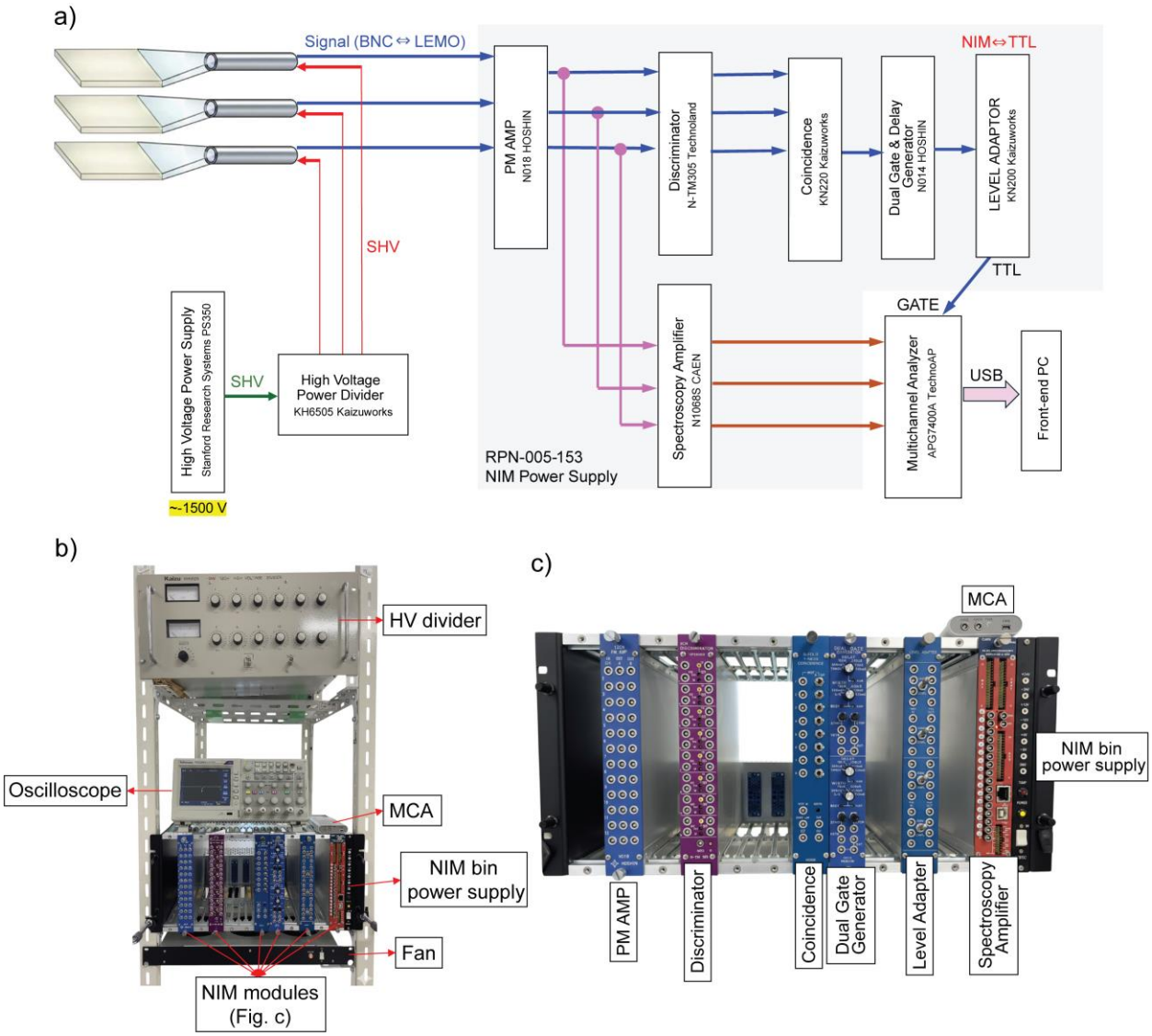


Figure 5 | Data acquisition and signal chain. (a) Block diagram of the electronics for muon detection. Analog PMT pulses split into two paths: a timing and trigger path with discriminator, threefold coincidence, gate and delay, and NIM to TTL level conversion; and a pulse-height path with a spectroscopy amplifier and a multichannel analyzer (MCA). The coincidence circuit issues a gate so that only valid threefold events are accumulated for pulse-height spectra and MIP selection. (b) Photograph of the complete DAQ rack showing the high-voltage divider, oscilloscope, MCA, NIM bin power supply, cooling fan, and the NIM module crate. (c) Close-up of the NIM module crate showing the PM amplifier, discriminator, coincidence, dual gate generator, level adapter, and spectroscopy amplifier.

Event Selection

Muon candidates were selected with a data-driven pulse-height window around the minimum-ionizing (MIP) peak on each channel's spectrum[53,54]. We locate the peak using a smoothed search (Savitzky–Golay filter[55,56]) and bound it by a left "valley" minimum and a right threshold that excludes the high-ADC Landau tail[3,54]. The same automatic windowing is applied to all runs (background, acrylic stacks, blind targets). Figure 6 illustrates a typical selected MIP region. Details of the smoothing and selection method are in the supplementary information (Figs. 2 and 3). The code for the MIP selection process and sample experiment output files are available on an online repository.

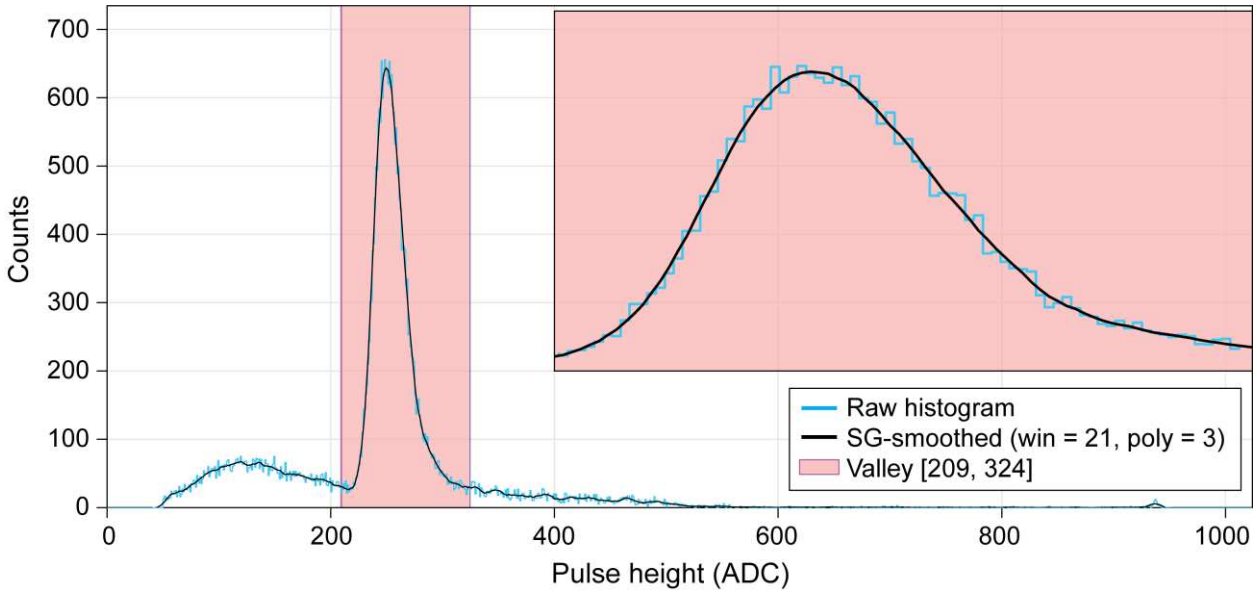


Figure 6 | Pulse-height spectrum. Raw histogram (blue steps) and Savitzky–Golay smoothed curve (black; window = 21, polynomial order = 3). The shaded region denotes the selected MIP valley $[ADC_{left}, ADC_{right}]$.

Real-time normalization (dual) and single-telescope baseline

Simultaneous operation cancels common-mode flux changes by forming the hourly ratio

$$T_{dual}(t) = \frac{R_{main}(t)}{R_{ref}(t)}, \quad (3)$$

where R_{main} and R_{ref} are MIP-selected counts per hour (CPH). A 140-hour no-target run provides a cross-calibration factor as

$$C_{cal} = \langle T_{dual}(t) \rangle_{\text{no target}}\,, \tag{4}$$

which absorbs small efficiency/acceptance differences. Sample transmissions are then computed as the corrected ratio

$$T(t) = \frac{T_{dual}(t)}{C_{cal}}\,, \tag{5}$$

and summarized by the time average $\langle T \rangle$ with uncertainty given by the standard error of the mean (SEM). The effective linear attenuation coefficient for a sample with a thickness of x is calculated using:

$$\mu = -\frac{1}{\mathrm{x}} \ln\langle T_s \rangle\,, \tag{6}$$

For comparison, we also form a conventional single-telescope estimator that uses the main telescope only,

$$T_{single}(t) = \frac{R_{main}(t)}{R_{0,\,main}}\,, \tag{7}$$

where $R_{0\,\mathrm{main}}$ is the main-telescope rate from its sequential background run. This baseline assumes stationarity of the incident muon flux between runs. Reported uncertainties propagate counting statistics and, respectively, the dispersion of C_{cal} (dual) or of $R_{0\,\mathrm{main}}$ (single).

Transmission model and density mapping

Stacked acrylic slabs ($\rho_{\mathrm{acrylic}} = 1.20\ \mathrm{gcm}^{-3}$) with path lengths $x \in (20, 40, 60, 80)$ cm provide an empirical calibration of the transmission–thickness relation,

$$T(x) = Ae^{-\mu x}\,, \tag{8}$$

fitted by weighted least squares using pointwise SEMs. For any target s of thickness d_s and measured mean transmission $\langle T_s \rangle$ (computed either with the dual estimator or with the single estimator), we map to an equivalent acrylic thickness and density via the following equations.

$$d_{equiv,s} = -\frac{1}{\mu} \ln\left(\frac{\langle T_s \rangle}{A}\right), \tag{9}$$

$$\rho_s = \rho_{acrylic} \frac{d_{equiv}}{d_s}, \tag{10}$$

Uncertainties on ρ_s propagate the SEM on $\langle T_s \rangle$ together with the (A, μ) covariance from the acrylic fit. A Bayesian reanalysis yielded concordant central estimates with modestly larger uncertainties, indicating robustness to the choice of estimator. Figure. 7a shows a sample of an 80 cm thick acrylic measurement, and Figs. 7b and 7c represent the bind test measurements of aluminum and stainless steel, respectively. The workflow for density estimation is summarized in Supplementary Information Figure 4.

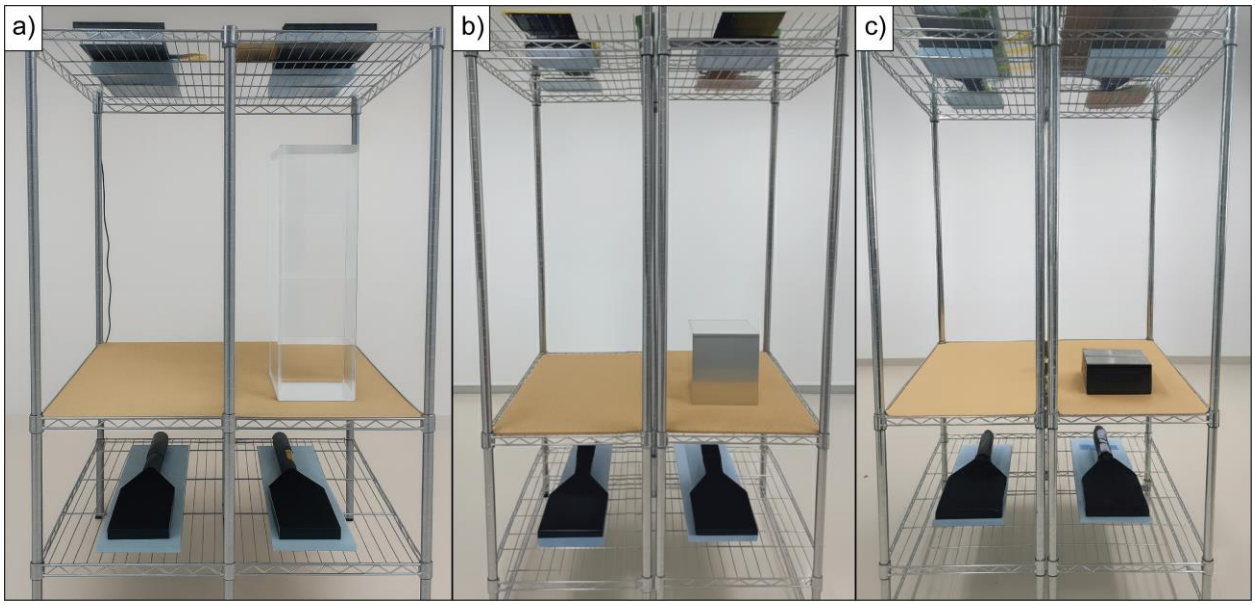


Figure 7 | Acrylic calibration geometry for constructing $\boldsymbol{T(x)}$ and blind targets used to validate density retrieval. (a) Four stacked 20 cm thick acrylic slabs are aligned with the 20 × 20 cm² scintillator aperture, providing path lengths $x = 20, 40, 60,$ and 80 cm. During all runs, the reference telescope viewed open sky. In all configurations, the test block fully covered the main telescope's 20 × 20 cm² aperture. The target densities were treated as unknowns, and the retrieved values were compared against nominal references. (b) Aluminum blind target, 20 × 20 × 20 cm³ ($d = 20$ cm). (c) Stainless steel blind target, 20 × 20 × 10 cm³ ($d = 10$ cm).

Alignment test

To assess the effects of geometry on common-mode rejection, we repeated a long background run with the two telescopes stacked vertically (as depicted in Fig. 8, referenced above the main text) and compared it against the side-by-side layout, using identical selection and time binning. The vertical stack increased hour-scale coherence and reduced scattering in the calibration ratio.

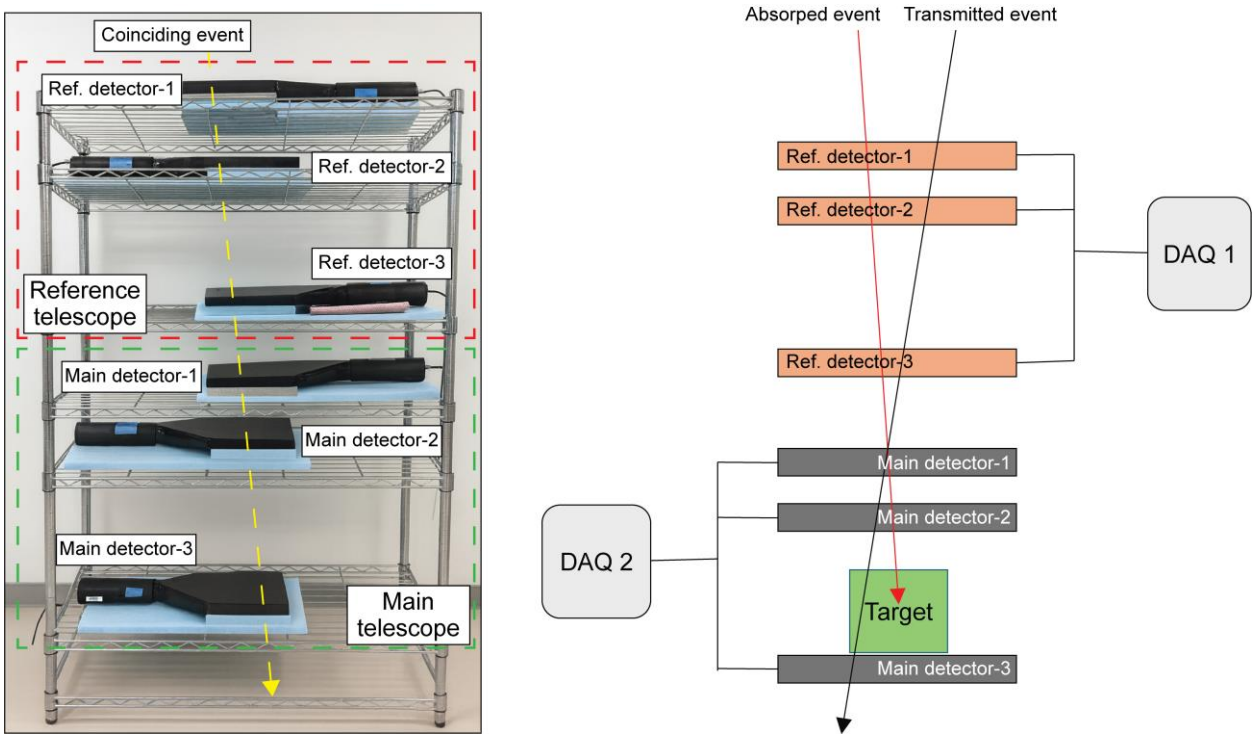


Figure 8 | Vertically stacked configuration for alignment testing. The reference telescope is mounted directly above the main telescope to enhance common-mode noise rejection during alignment verification.

Dataset availability

The dataset and codes that support the findings of this study are available from the corresponding author upon reasonable request.

Code availability

The code for the MIP selection process and sample experiment output files is available on an online repository: https://github.com/hamidb90/MIPselection.

References

1 Gaisser, T. K., Engel, R. & Resconi, E. *Cosmic rays and particle physics*. (Cambridge University Press, 2016).
2 Bonechi, L., D'Alessandro, R. & Giammanco, A. Atmospheric muons as an imaging tool. *Reviews in Physics* **5**, 100038 (2020).
3 Knoll, G. F. *Radiation detection and measurement*. (John Wiley & Sons, 2010).
4 Scampoli, P. & Ariga, A. *Cosmic ray muography*. (World Scientific, 2023).
5 Borozdin, K. N. *et al.* Radiographic imaging with cosmic-ray muons. *Nature* **422**, 277-277 (2003).

6 Oláh, L., Tanaka, H. K. & Varga, D. *Muography: Exploring Earth's subsurface with elementary particles*. (John Wiley & Sons, 2022).
7 NAGAMINE, K. Geo-tomographic observation of inner-structure of volcano with cosmic-ray muons. *Journal of Geography (Chigaku Zasshi)* **104**, 998-1007 (1995).
8 Tanaka, H. K. Japanese volcanoes visualized with muography. *Philosophical Transactions of the Royal Society A* **377**, 20180142 (2019).
9 Nishiyama, R. *et al.* Integrated processing of muon radiography and gravity anomaly data toward the realization of high-resolution 3-D density structural analysis of volcanoes: Case study of Showa-Shinzan lava dome, Usu, Japan. *Journal of Geophysical Research: Solid Earth* **119**, 699-710 (2014).
10 Tanaka, H. K. *et al.* Detecting a mass change inside a volcano by cosmic-ray muon radiography (muography): First results from measurements at Asama volcano, Japan. *Geophysical Research Letters* **36** (2009).
11 Schouten, D. Muon geotomography: selected case studies. *Philosophical Transactions of the Royal Society A* **377**, 20180061 (2019).
12 Beni, T. *et al.* Transmission-based muography for ore bodies prospecting: A case study from a Skarn Complex in Italy. *Natural Resources Research* **32**, 1529-1547 (2023).
13 Bonneville, A. *et al.* Borehole muography of subsurface reservoirs. *Philosophical Transactions of the Royal Society A* **377**, 20180060 (2019).
14 Alvarez, L. W. *et al.* Search for Hidden Chambers in the Pyramids: The structure of the Second Pyramid of Giza is determined by cosmic-ray absorption. *Science* **167**, 832-839 (1970).
15 Morishima, K. *et al.* Discovery of a big void in Khufu's Pyramid by observation of cosmic-ray muons. *Nature* **552**, 386-390 (2017).
16 Giammanco, A. *et al.* Toward using cosmic rays to image cultural heritage objects. *iScience* **28** (2025).
17 Lagrange, M. *et al.* Muon tomography for cultural heritage objects. *Journal of Applied Physics* **138** (2025).
18 Guardincerri, E. *et al.* 3D cosmic ray muon tomography from an underground tunnel. *Pure and Applied Geophysics* **174**, 2133-2141 (2017).
19 Oláh, L., Tanaka, H. K., Mori, T., Sakatani, Y. & Varga, D. Structural health monitoring of sabo check dams with cosmic-ray muography. *Iscience* **26** (2023).
20 Basiri, H., Kin, T., Okamoto, N., Giammanco, A. & Gil, E. C. Simulation of a First Case Study for Magnetic Field Imaging with the Magic-μ Technique. *Journal of Advanced Instrumentation in Science* (2022).
21 Kin, T., Basiri, H., Gil, E. C. & Giammanco, A. Magnetic Field Imaging by Cosmic-Ray Muons (Magic-μ): First Feasibility Simulation for Strong Magnetic Fields. *Journal of Advanced Instrumentation in Science* (2023).
22 Kudryavtsev, V. A., Spooner, N. J., Gluyas, J., Fung, C. & Coleman, M. Monitoring subsurface CO2 emplacement and security of storage using muon tomography. *International journal of greenhouse gas control* **11**, 21-24 (2012).
23 Gluyas, J. *et al.* Passive, continuous monitoring of carbon dioxide geostorage using muon tomography. *Philosophical Transactions of the Royal Society A* **377**, 20180059 (2019).
24 Bryman, D. *et al.* Muon Geotomography—Bringing New Physics to Orebody Imaging. (2014).
25 Pang, J. *et al.* Accurate in situ rock density measurement with cosmic ray muon radiography. *Journal of Applied Physics* **135** (2024).
26 Jonkmans, G., Anghel, V., Jewett, C. & Thompson, M. Nuclear waste imaging and spent fuel verification by muon tomography. *Annals of Nuclear Energy* **53**, 267-273 (2013).
27 Miyadera, H. *et al.* Imaging Fukushima Daiichi reactors with muons. *Aip Advances* **3** (2013).
28 Procureur, S. *et al.* 3D imaging of a nuclear reactor using muography measurements. *Science Advances* **9**, eabq8431 (2023).

29 Lesparre, N. *et al.* Design and operation of a field telescope for cosmic ray geophysical tomography. *Geoscientific Instrumentation, Methods and Data Systems* **1**, 33-42 (2012).
30 Cimmino, L. *et al.* A new cylindrical borehole detector for radiographic imaging with muons. *Scientific Reports* **11**, 17425 (2021).
31 Baccani, G. *et al.* The MIMA project. Design, construction and performances of a compact hodoscope for muon radiography applications in the context of archaeology and geophysical prospections. *Journal of Instrumentation* **13**, P11001 (2018).
32 Al Moussawi, M. *et al.* Simulation tools, first results and experimental status of the MURAVES experiment. (Fermi National Accelerator Laboratory (FNAL), Batavia, IL (United States), 2023).
33 Cohu, A. *et al.* First 3D reconstruction of a blast furnace using muography. *Journal of Instrumentation* **18**, P07004 (2023).
34 Saracino, G. *et al.* Imaging of underground cavities with cosmic-ray muons from observations at Mt. Echia (Naples). *Scientific reports* **7**, 1181 (2017).
35 Thompson, L. *et al.* Muon tomography for railway tunnel imaging. *Physical Review Research* **2**, 023017 (2020).
36 Ambrosino, F. *et al.* Joint measurement of the atmospheric muon flux through the Puy de Dôme volcano with plastic scintillators and Resistive Plate Chambers detectors. *Journal of Geophysical Research: Solid Earth* **120**, 7290-7307 (2015).
37 Anastasio, A. *et al.* The MU-RAY experiment. An application of SiPM technology to the understanding of volcanic phenomena. *Nuclear Instruments and Methods in Physics Research Section A: Accelerators, Spectrometers, Detectors and Associated Equipment* **718**, 134-137 (2013).
38 Pla-Dalmau, A., Bross, A. D. & Mellott, K. L. Low-cost extruded plastic scintillator. *Nuclear Instruments and Methods in Physics Research Section A: Accelerators, Spectrometers, Detectors and Associated Equipment* **466**, 482-491 (2001).
39 Son, J. *et al.* Improved 3D printing plastic scintillator fabrication. *Journal of the Korean Physical Society* **73**, 887-892 (2018).
40 Ambrosino, F. *et al.* The MU-RAY project: detector technology and first data from Mt. Vesuvius. *Journal of Instrumentation* **9**, C02029 (2014).
41 Kobelev, P., Hamraev, Y. B. & Yanke, V. Analysis of Meteorological Effects of Cosmic Ray Neutron Component Based on Data From Mid-Latitude Stations. *Solar-Terrestrial Physics* **10**, 99-105 (2024).
42 Agafonova, N. Y. *et al.* Characterization of the varying flux of atmospheric muons measured with the Large Volume Detector for 24 years. *Physical Review D* **100**, 062002 (2019).
43 Zaitseva, D. & Kokoulin, R. in *Journal of Physics: Conference Series.* 012029 (IOP Publishing).
44 Yanchukovsky, V. & Kuzmenko, V. Atmospheric effects of the cosmic-ray mu-meson component. *Solar-Terrestrial Physics* **4**, 76-82 (2018).
45 Jourde, K. *et al.* Monitoring temporal opacity fluctuations of large structures with muon radiography: a calibration experiment using a water tower. *Scientific reports* **6**, 23054 (2016).
46 Berkova, M. *et al.* Barometric Effect of High-Energy Muons (> 230 GeV).
47 Taricco, C. *et al.* Exploration of the stratosphere with cosmic-ray muons detected underground. *Physical Review Research* **4**, 023226 (2022).
48 Cane, H. V. Coronal mass ejections and Forbush decreases. *Space Science Reviews* **93**, 55-77 (2000).
49 Maghrabi, A., Al Harbi, H., Al-Mostafa, Z., Kordi, M. & Al-Shehri, S. The KACST muon detector and its application to cosmic-ray variations studies. *Advances in Space Research* **50**, 700-711 (2012).
50 Matsushima, J. *et al.* Joint measurement of cosmic-ray muons and seismic waves at laboratory scale. *Geophysical Journal International* **239**, 1821-1832 (2024).
51 Savić, M. *et al.* A novel method for atmospheric correction of cosmic-ray data based on principal component analysis. *Astroparticle Physics* **109**, 1-11 (2019).
52 Savić, M. *et al.* Modeling meteorological effects on cosmic ray muons utilizing multivariate analysis. *Space Weather* **19**, e2020SW002712 (2021).

53 Group, P. D. *et al.* Review of particle physics. *Progress of theoretical and experimental physics* **2022**, 083C001 (2022).
54 Leo, W. R. *Techniques for nuclear and particle physics experiments: a how-to approach*. (Springer Science & Business Media, 1994).
55 Savitzky, A. & Golay, M. J. Smoothing and differentiation of data by simplified least squares procedures. *Analytical chemistry* **36**, 1627-1639 (1964).
56 Sadeghi, M. & Behnia, F. Optimum window length of Savitzky-Golay filters with arbitrary order. *arXiv e-prints*, arXiv: 1808.10489 (2018).

Acknowledgments

This research was supported by the Mohammed bin Salman Center for Future Science and Technology for Saudi Arabia-Japan Vision 2030 at the University of Tokyo (MbSC2030) and by the Earthquake Research Institute, The University of Tokyo, (Grant No. ERI JURP 2024-H-03). AG received funding from the Fonds de la Recherche Scientifique - FNRS (Grant No. T.0129.25).

Author contributions

H.B. conceived and designed the study, developed the analysis software, performed the experiments and data acquisition, and prepared the figures with **A.E.** assisting in figure refinement. **J.M.** co-conceived the study and supervised the work. **M.Y.A.** contributed to conceptualization. **A.G.** and **E.C.G.** advised on methodology and validation. **M.K.**, **T.Y.**, **M.Y.A.**, **F.B.**, and **A.E.** contributed to the investigation. **H.K.M.T.** and **J.M.** acquired funding and administered the project. **H.B.** wrote the first draft; all authors discussed the results and revised the manuscript.

Competing interests

The authors declare no competing interests.

Supplementary Files

This is a list of supplementary files associated with this preprint. Click to download.

- SupplementaryInformationv4.docx